applied sciences

MDPI

Article

A Novel Approach to Tele-Ultrasound Imaging: Compressive Beamforming in Fourier Domain for Ultrafast Ultrasound Imaging

Xinyu Zhang [1,2], Yiwen Xu [1,2], Ninghao Wang [1,2], Yang Jiao [2,*] and Yaoyao Cui [2,*]

[1] The School of Biomedical Engineering (Suzhou), Division of Life Sciences and Medicine, University of Science and Technology of China, Suzhou 215163, China
[2] The Suzhou Institute of Biomedical Engineering and Technology, Chinese Academy of Sciences, Suzhou 215163, China
* Correspondence: jiaoy@sibet.ac.cn (Y.J.); cuiyy@sibet.ac.cn (Y.C.)

Abstract: Tele-ultrasound imaging is useful in various situations. Plane wave imaging provides a method for ultrafast ultrasound with very high frame rates, which sacrifices image quality and leads to the problem of a large amount of data and low signal transmission speed in telemedicine imaging. In this paper, a novel compressive frequency-wavenumber domain beamforming method is introduced, which integrates Stolt's f-k method and compressed sensing theory on the lateral wavenumber. The data load is reduced by the sparsity of the echo signal parallel to the transducer, which requires a smaller measurement matrix during compressed sensing to reduce memory usage and accelerate the transmission rate. The signal is compressed in the Fourier domain to obtain greater stability and better image quality after reconstruction than if it was compressed in the temporal domain. Simulated data and experimental acquisitions were used to compare compressive Fourier domain beamforming with conventional delay-and-sum (DAS) beamforming. The results showed that compressive beamforming within the wavenumber domain provides the image with higher quality from less data.

Keywords: telemedicine imaging; beamforming; compressed sensing; ultrasound ultrafast imaging; Stolts's migration

check for updates

Citation: Zhang, X.; Xu, Y.; Wang, N.; Jiao, Y.; Cui, Y. A Novel Approach to Tele-Ultrasound Imaging: Compressive Beamforming in Fourier Domain for Ultrafast Ultrasound Imaging. *Appl. Sci.* **2023**, *13*, 3127. https://doi.org/10.3390/app13053127

Academic Editor: Alessandro Ramalli

Received: 15 February 2023
Revised: 24 February 2023
Accepted: 27 February 2023
Published: 28 February 2023

1. Introduction

Ultrasound imaging has been widely used in clinical disease diagnosis and treatment evaluation due to its non-invasive, real-time, and cost-effective characteristics. Tele-ultrasound imaging is also an important part of telemedicine imaging. Telemedicine has evolved in the last few years to improve healthcare system not only for patient outcomes, but also for education purpose [1]. The obstetric tele-ultrasound has been proved feasible with a bandwidth of 2 Mbit/s video link [2]. Transmission of real-time ultrasound video to a remote iPhone with a WiFi connection and a 3G connection were both accomplished. However, the frame rate was reduced to 1.1 frames/s from 11.9 frames/s of the original transmitted signal [3]. In order to obtain better image quality and higher frame rate in telemedicine imaging, the amount of data can be reduced, in addition to increasing the network bandwidth.

B-mode ultrasound imaging is currently the most widely used clinical ultrasound diagnostic methods. Traditional B-mode imaging has a frame rate of 30–40 frames/s, which can meet the requirements of observing the static physiological structure of tissues, such as imaging of the liver, kidney, and abdomen. With the development of more medical ultrasound technologies, such as shear wave elastography [4], cardiac imaging, ultrasound localization microscopy (ULM) [5], etc., higher requirements are placed on the frame rate of ultrasound imaging. Methods to augment the frame rate of ultrasound imaging include multi-line-transmit/receive method, synthetic aperture emission imaging and wide beam emission imaging [6]. Wide beam imaging is a novel transmission method of ultrasound, which includes plane waves and divergent waves. A single plane wave transmission of ultrasound can cover the entire imaging area, and then the full aperture receives and records the echo signal in order to produce an ultrasound image [7]. At present, plane wave imaging can obtain the entire image through a single full-aperture transmit-receive, which can increase the frame rate to more than 10,000 frames/s [8]. It has been applied to shear wave elastography [9], brain function imaging [10], and ultrasound localization microscopy [5].

Compared with the focused wave scanning transmission method, the plane wave transmission method greatly increases the frame rate. However, the signal-to-noise ratio, the image resolution and the contrast of the echo signal are deteriorated because the transmitting beam is not focused. The imaging results of a plane wave emitted once have the problems of poor resolution and low signal-to-noise ratio. In practical applications, multi-angle compound imaging methods are often used [9]. The multi-angle compound imaging mode improves imaging quality with the increase of the angle, but the frame rate will linearly decrease in this way as well. In order to retain the advantages of plane wave imaging's high frame rate as much as possible, different beamforming algorithms are applied to plane wave imaging to improve image quality without reducing the frame rate.

Currently, the commonly used beamforming methods are delay-and-sum (DAS) and adaptive beamforming algorithm based on minimum variance (MV) [11]. The DAS algorithm is the most basic beamforming algorithm, which applies the fixed weights to the echo signal after delay processing to reduce the signal side lobes. However, the weight of the window function used in the traditional amplitude apodization process is usually a set of fixed parameters preset according to the depth. Therefore, the sidelobe attenuation is at a certain degree, and the width of the main lobe will also increase, that is, the resolution will not improve [12]. Compared with DAS, the adaptive beamforming uses the signal received by the transducer to adaptively calculate the weighting value added to each element. Because this weighting value is dynamic, it has better resolution and anti-interference ability [13]. However, the MV method of beamforming involves lots of matrix operation which augment the computation complexity, due to the calculation of correlation matrix. Roya et al. proposed a compressive sensing-based approach combined with the combination of the adaptive minimum variance (MV) algorithm to reduce computational burden [14]. Deep learning is an emerging method for beamforming [15]. Different neural networks are used to improve image quality or to augment imaging speed in beamforming [16,17]. However, this algorithm often requires a lot of data for training or has a high computational complexity, which is not suitable for high -frequency imaging in practical settings. Compared with algorithms based on MV, DAS requires a relatively small amount memory in the temporal domain because there is no matrix computation. Lu [18] introduced the plane wave imaging process to the Fourier domain, which provided a new direction for beamforming. Compared with beamforming methods in the temporal domain, beamforming in the Fourier domain might augment computational efficiency by applying fast Fourier transform (FFT) [19]. Lu [18] introduced the mapping method to coordinate the echo signal from temporal spectrum to frequency-wavenumber space, which achieved to beamform in wavenumber-space. Bernard et al. [20] proposed a novel remapping method related to the steered angle in reception. After that, Garcia et al. [21] proposed a beamforming process in the Fourier domain based on the exploding reflector model (ERM), which is widely used in seismology [22]. Compared with Lu's method, this model assumes that the echo waves of the backscatters only propagate in the direction of the sensor, so that the principle of Stolt's migration is different from the model proposed by Lu. This model is closer to the reality, thus improving imaging quality. Then Chen et al. [23] modified the structure of the algorithm by aligning coordinates before the axial inverse fast Fourier transform (IFFT) and the lateral IFFT, which enables direct coherent compounding in the Fourier domain. Based on f-k migration, a circular statistics vector (CSV) was used as a weighted factor to achieve better image quality [24].

High imaging frame rate will lead to the problem of large data load and memory storage. Moreover, a large amount of data also reduces the transfer speed which limits transmission speed in telemedicine imaging. Compressed Sensing (CS) is a new sampling theory, which allows the signal to be sampled under the Nyquist sampling rate [25]. This theory is based on the signal's sparsity, which means the original signal can be randomly sampled to obtain discrete samples. There is only a small amount of non-zero information in this discrete sample. The sample can be reconstructed to the original signal by a recovery algorithm with high quality. Compressed sensing has been widely used in data acquisition [26], radar [27] and the communication field. Wang et al. [28] and Szasz et al. [29] considered the transmitted ultrasonic signal as an impulse to form a sparse measurement matrix with a large number of zero-elements to reduce memory usage. Then, wavelet sparsity was introduced to the recovery algorithm to reconstruct the image. Chernyakova et al. [30,31] proposed a CS-based Fourier beamforming with a Xampling scheme for undersampling. Besson et al. [32] firstly joint compressed sensing with beamforming in the wavenumber domain. Although compressed sensing allows the signal to be sampled at a sampling rate lower than the Nyquist sampling rate, the measurement matrix occupies lots of memory as well. Reducing transducer elements is an effective method in DAS to reduce the data load with a small measurement matrix [33].

In this paper, we propose a new framework based on Stolt's f-k and compressed sensing theory, which is a compressive beamformer in the wavenumber domain, to obtain a smaller amount of data load during signal transmission and better image quality in telemedicine. We introduce compressed sensing to the frequency-wavenumber domain, which reduce data load for transmission and memory storage, as well as maintaining the image quality and stability compared with that in the temporal domain.

This paper is stated as follows: Section 2 introduced the modified Stolt's f-k method and compressed sensing theory in the wavenumber domain at first. Then, beamforming in the frequency-wavenumber domain and compressed sensing are combined to assemble the novel framework: compressive beamformer in the wavenumber domain. In Section 3, simulated data and experimental acquisitions are used in the new framework to compare with DAS and compressive beamformer in the temporal domain. In Section 4, the influence of compounding angles on image qualities of different beamformers are discussed. Moreover, memory occupation, computational complexity and telemedicine imaging speed are discussed. Section 5 provides a conclusion of the novel compressive wavenumber domain beamforming framework.

2. Materials and Methods

2.1. Plane Wave Stolt's f-k Method

Stolt's f-k beamforming method was first proposed based on the exploding reflector model (ERM), and was widely used in seismic imaging and other fields. Garcia et al. [21] applied Stolt's f-k method to ultrasonic plane wave imaging. In seismology, the ERM model assumes that all sound sources in the underground imaging area generate sound waves at the same time, and the sound waves only propagate upward. In order to apply the Stolt's f-k method to ultrasonic plane wave imaging, Garcia et al. [21] first demonstrated that the ERM model can be transformed into plane waves at different angles. Under the premise of the same echo signal, if the real scatterer position in the plane wave is obtained, the corresponding virtual scatterer position in the ERM model can be calculated according to the conversion method. On this basis, Garcia et al. [21] used Stolt's f-k method to process plane wave signals at various angles, and obtained the virtual scatterer position under the ERM model. Then the real scatterer position can be calculated by the migration principle. Coherent compound imaging can be implemented by correcting delay and aligning spectrum's coordinates of different angles.

Shown as Figure 1, for the plane wave emitted with an angle of θ, the longitudinal position of the inclined echo signal due to the emission angle will be distorted. Before using the Stolt's f-k method, the position of received RF data should be corrected at first. We assume that (x_s, z_s) is the position of a scatterer, then the travel time of echo signal is:

$$\tau_s(x) = \frac{1}{c}(\sin(\theta)(x_s - x) + \cos(\theta)z_s + \sqrt{(x_s - x)^2 + z_s{}^2}) \tag{1}$$

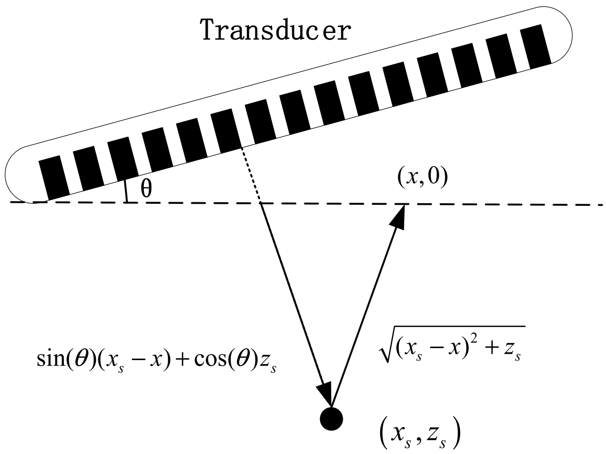

Figure 1. Scheme of route for the echo signal travelling from transmitter to receiver.

The signal travels from emitter to scatterer and back to the receiver, depending on the transducer position $(x, 0)$. To be compatible with the ERM model, the virtual exploding source is positioned at $(\hat{x}_s, \hat{z}_s)$ with a propagation speed of $\hat{c}$. $\hat{c}$ is a one-way speed from scatterer to the receiver. Then the following ERM travel time is:

$$\hat{\tau}_s(x) = \frac{1}{\hat{c}}\sqrt{(\hat{x}_s - x)^2 + \hat{z}_s^2} \tag{2}$$

By equalizing $\tau_s(x)$ and $\hat{\tau}_s(x)$, the relationships of the sound speed and coordinates between real situation and that in ERM model are obtained by the coefficients as below:

$$\hat{\tau}_s(x) = \frac{1}{\alpha c}\sqrt{(x_s + \gamma z_s - x)^2 + \beta^2 z_s{}^2} \tag{3}$$

where (α, β, γ) are defined as follows:

$$\begin{cases} \alpha = 1/\sqrt{1 + \cos(\theta) + \sin^2(\theta)} \\ \beta = \frac{(1+\cos(\theta))^{3/2}}{1+\cos(\theta)+\sin^2(\theta)} \\ \gamma = \frac{\sin(\theta)}{2-\cos(\theta)} \end{cases} \tag{4}$$

In the equation, α relates the virtual propagation speed $\hat{c}$ and real speed c. β represents the scaling ratio between the virtual axial coordinate $\hat{z}_s$ and the real axial depth z_s. γ refers to the shift operation between virtual lateral coordinate $\hat{x}_s$ and real lateral position x_s. The relationship between virtual arguments and actual arguments are shown as follow:

$$\begin{cases} \hat{c} = \alpha c \\ \hat{z}_s = \beta z_s \\ \hat{x}_s = x_s + \gamma z_s \end{cases} \tag{5}$$

Assume that a plane wave is emitted at the angle of θ, and the RF data of the echo signal is ψ_θ. If the plane wave is backscattered in receiving, the signal received at the probe whose coordinate is $(x, z = 0)$ can be present as $\psi_\theta(x, z = 0, t)$. Fourier transform is applied to $\psi_\theta(x, z = 0, t)$ over time t to obtain the spectrum $G_\theta(x, z = 0, f)$, where f is the temporal frequency. Because of the time delay $\tau(x)$ in the temporal domain, the Fourier transform should be followed by a phase shift $e^{i2\pi \sin(\theta)x/c}$ in the frequency domain, as follows:

$$G_\theta(x, z = 0, f) = \int_{-\infty}^{+\infty} \psi_\theta(x, z = 0, t) e^{-i2\pi f t} e^{i2\pi \sin(\theta)x/c} dt \tag{6}$$

Then the phase-shifted spectrum is Fourier transformed in the lateral dimension

$$G_\theta(k_x, z = 0, f) = \int_{-\infty}^{+\infty} G_\theta(x, z = 0, f) e^{-i2\pi k_x x} dx \tag{7}$$

where k_x refers to the lateral spatial wavenumber on the transducer surface. Chen et al. [23] modified the process of beamforming by applying the phase shift once before lateral FFT, instead of applying another phase shift after migration.

The core of the spectrum migration is to estimate initial spectrum $\phi_\theta(k_x, k_z, t = 0)$ from the obtained spectrum $G_\theta(k_x, z = 0, f)$ as the boundary condition. $\phi_\theta(k_x, k_z, t = 0)$ is the Fourier transform over actual coordinate (x_s, z_s). This procedure can be divided into two steps. The first is mapping $G_\theta(k_x, 0, f)$ to $\hat{\phi}_\theta(k_x, k_z, 0)$, where $\hat{\phi}_\theta(k_x, k_z, 0)$ refers to Fourier transform over virtual source $(\hat{x}_s, \hat{z}_s)$. The second step is to shift $\hat{\phi}_\theta(k_x, k_z, 0)$ to $\phi_\theta(k_x, k_z, 0)$.

To map $G_\theta(k_x, 0, f)$ to $\hat{\phi}_\theta(k_x, k_z, 0)$, Garcia et al. [21] provided the solution as

$$\hat{\phi}_\theta(k_x, k_z, 0) = \frac{\hat{c} k_z}{\sqrt{{k_x}^2 + {k_z}^2}} G_\theta(k_x, 0, f(k_x, k_z)) \tag{8}$$

where k_z is the axial spatial wavenumber perpendicular to the transducer k_x and k_z are related to f by

$$f = \hat{c} sign(k_z) \sqrt{{k_x}^2 + {k_z}^2} \tag{9}$$

Then $\hat{\phi}_\theta(k_x, k_z, 0)$ should be transformed to $\phi_\theta(k_x, k_z, 0)$ for Fourier transform of the real coordinates.

$$\phi_\theta(k_x, k_z, 0) = \hat{\phi}_\theta(k_x, (k_z - k_x \gamma)/\beta, 0) \tag{10}$$

$\phi_\theta(k_x, k_z)$ is the Fourier transform over actual coordinates. Then the final image can be obtained by applying 2-D Fourier inverse transform over $\phi_\theta(k_x, k_z)$

$$\psi_\theta(x, z) = \int \int_{-\infty}^{+\infty} \phi_\theta(k_x, k_z) e^{2i\pi(k_x x + k_z z)} dk_x dk_z \tag{11}$$

$\psi_\theta(x, z)$ is the final image data after beamforming. This procedure augments computational speed because it replaces time-delay calculation with FFT in the Fourier domain. This model assumes that the reflected sound wave of the scatterers only propagates in the direction of the sensor, which makes the principle of spatial spectrum coordinate migration different from the model proposed by Lu [18]. In reflective ultrasound equipment, the performance of the scatterers as a reflection model is more suitable to the actual situation than the pure scattering model, so this method improves the imaging quality.

2.2. Proposed Compressed Sensing Process in the Wavenumber Domain

The transducer with N elements emits a plane wave signal, which equals the number of lateral numbers. The raw data of echo signal is $\psi_\theta(x, z, t)$ in the temporal domain. The echo signal is transferred to $G_\theta(k_x, z, f)$ in the Fourier domain by 2D-dimensioan FFT. The ultrasonic echo signal in the wavenumber domain can express sparsity by a transfer matrix based on directivity vector. To avoid large transfer matrix, we compress the data load by k_x. According to compressed sensing theory, the transfer matrix can be established by the number of transducer elements and size of the transfer matrix. To ensure that the projection vector is sparse, which means there are only few elements non-zero, the number of the rows of the transfer matrix should be less than columns. The projection coefficient vector is obtained by projecting the echo signal on the transfer matrix. Then the echo signal of all transducer elements can be expressed as follows

$$G_\theta(k_x) = \mathrm{H}S(k_x) \tag{12}$$

where H is the transfer matrix. $S(k_x)$ is the projection coefficient vector where echo signal $G_\theta(k_x)$ project on transfer matrix H. There are only few non-zero elements in the vector $S(k_x) = [0, 0, \cdots, s_1(k_x), 0, \cdots, 0, s_K(k_x), 0, \cdots, 0]$, namely $S(k_x)$ is sparse. The transfer matrix H can be constructed as follows to make the echo signal in the wavenumber domain $G_\theta(k_x)$ sparse.

Divide the space $[-90°, 90°]$ into $2N$ parts on average to obtain $\varphi_k = k\pi/N$ and establish directivity vector $\delta(\varphi_k)$ as follow

$$\delta(\varphi_k) = [1, e^{-i2\pi d \sin(\varphi_k)/\lambda}, e^{-i2\pi 2d \sin(\varphi_k)/\lambda}, \cdots, e^{-i2\pi(N-1)d \sin(\varphi_k)/\lambda}]^T \tag{13}$$

where d is the kerf between elements of the transducer. λ is wavelength of the plane wave. Directivity vector can be regarded as the sparse base to construct transfer matrix. Then the transfer matrix is

$$\mathrm{H} = [\delta(\varphi_1), \delta(\varphi_2), \cdots, \delta(\varphi_{2N})] \tag{14}$$

In order to compress signal $G_\theta(k_x)$, we would like to obtain $S(k_x)$ by constructing measurement matrix and re-weight minimum-focal underdetermined system solver algorithm (RM-FOCUSS) [34]. Compressed sampling is not a direct measurement of $G_\theta(k_x)$, but a design of a $M \times N (M < N)$ dimensional sampling matrix $\Lambda = [\kappa_1, \kappa_2, \cdots, \kappa_M]$, which is uncorrelated to the transfer matrix H. The projection vector $Z(k_x)$ of $G_\theta(k_x)$ on Λ is

$$Z(k_x) = \Lambda G_\theta(k_x) = \Lambda \mathrm{H} S(k_x) \tag{15}$$

Sampling matrix Λ represents the compressed sampling method of the echo signal, which is composed of M sampling bases. Each sampling base is an N-dimension vector, such as $\kappa_i = [\kappa_{i1}, \kappa_{i2}, \cdots, \kappa_{iN}]$. The i-th row means that the output of all the transducer elements is projected onto the sampling base, corresponding to a compressed sampling point. The sampling matrix Λ has M rows in total, which means that only M compressed sampling points are needed. M transducer elements can be selected for sampling from the N transducer elements of the original array.

The matrix $\mathrm{P} = \Lambda\mathrm{H}$ in [15] is an $M \times 2N$ matrix, which is called the measurement matrix. The measurement matrix is used to sample the observations so that the original signal can be reconstructed. Theoretical studies [35] have shown that when the measurement matrix P satisfies the restricted isometry property (RIP) condition, the projection coefficient vector $S(k_x)$ can be solved, and the original signal $G_\theta(k_x)$ can be reconstructed accurately by the compressed sampling vector $Z(k_x)$. This property ensures that the original space has a one-to-one mapping relationship to the sparse space, which requires that the sampling matrix randomly selected from the observation matrix must be non-singular. The measurement matrix can measure the signal to obtain the measurement vector, and then use the reconstruction algorithm to reconstruct the full signal from the measured value. When designing the measurement matrix, it is required that the measured value will not affect the information of the original signal during the sparse expression of the signal, so as to ensure that the signal can be accurately reconstructed. The theory proves that the Gaussian random sampling matrix and any fixed transformation matrix can make P satisfy the RIP condition with a high probability [36], and the Gaussian random matrix can be easily obtained, so this paper adopts the Gaussian random measurement matrix.

The process to design a sampling matrix Λ is as Figure 2 [33]:

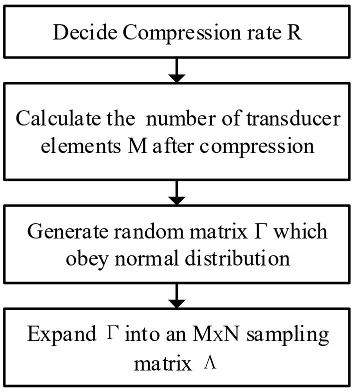

Figure 2. The process of designing a sampling matrix.

Define $Y(k_x) = [y_1(k_x), y_2(k_x), \cdots, y_M(k_x)]$ as the output of the compressed sampling array elements. The compressed sampling vector is

$$Z(k_x) = \Gamma Y(k_x) = \mathrm{PS}(k_x) \tag{16}$$

After obtaining the compressed sample vector $Z(k_x)$, the re-weight minimum-focal underdetermined system solver algorithm (RM-FOCUSS) [34] is used to estimate the projection coefficient vector $S(k_x)$. Then the original signal $G_\theta(k_x)$ can be reconstructed by [12].

For L plane wave emitted from transducer, the cost function J is established as follow in order to obtain the sparse signal $S(t)$

$$J^{(p)}(S) = \sum_{i=1}^{2N} \left(\sum_{l=1}^{L} |s_{i,l}|^2 \right)^{p/2} \tag{17}$$

when p is closer to 0, the $S(k_x)$ expressed by $J^{(p)}(S)$ is more sparse. The Lagrange operator is defined as

$$L(S, \Omega) = J^{(p)}(S) + \sum_{l=1}^{L} \omega_l{}^T (\mathrm{PS}[:, l] - Z[:, l]) \tag{18}$$

where ω_l is Lagrange operator vector, $l = 1, 2, \cdots L$. $S(t)$ can be obtained by minimum Lagrange operator $L(S, \Omega)$. The solution of RM-FOCUSS algorithm was proposed in [34] as follow

$$\left.\begin{array}{l} W_{k+1} = diag\left[c_k[i]^{1-p/2}\right] \\ c_{k+1}[i] = \|s_k[i,:]\| = \left[\sum_{l=1}^{L}\left(s_k[i,l]^2\right)\right]^{1/2}, p \in [0,2] \\ S_{k+1} = W_{k+1}(PW_{k+1})^H\left((PW_{k+1})(PW_{k+1})^H + \sigma I\right)^{-1} Z \end{array}\right\} \tag{19}$$

where p is related to the sparsity of echo signal. σ is a parameter reflecting the noise. We could eliminate part of the noise by adjusting σ. After the RM-FOCUSS algorithm, we obtain the sparse signal $S(k_x)$. This sparse signal is the compressed solution after compressed sensing because of lots of zero elements. Finally, apply [12] to obtain the full-array signal. This signal is no longer the original signal but with some amelioration and modification, whether all the information can be recovered and whether the noise can be eliminated depending on the performance of this compressed sensing process.

The beamforming based on compressed sensing can become a method of sparsity by reducing the number of transducer elements without reducing the image performance. It uses the sparseness of the ultrasonic signal to randomly extract part of the signals from the transducer, restores the original signal with a restoration algorithm, and then performs beamforming. In beamforming based on the compressed sensing, the transfer matrix, the sampling matrix and the sparsity solution algorithm all influence whether the reconstructed signal can retain all the image information.

2.3. Wavenumber Domain Compressive Beamforming

To improve the compressed rate without sacrificing image quality, we propose the framework to combine compressed sensing with beamforming in the frequency-wavenumber domain. According to the characteristic of ultrasonic signal, the energy of the echo signal concentrates on low frequency. Assume that $\psi_\theta(x, z = j, t)$ represents the j-th line of the RF data of echo signal. To transform the echo signal to the frequency-wavenumber domain, the spectrum can be expressed as follows

$$G_\theta(x, z = j, f) = \int_{-\infty}^{+\infty} \int_{-\infty}^{+\infty} \psi_\theta(x, z = j, t) e^{-i2\pi f t} e^{-i2\pi k_x x} dt dx \quad (20)$$

After transforming the echo signal into the frequency-wavenumber domain, the spectrum of signal parallel to the transducer direction become symmetric because of the characteristic of FFT. We choose the 32nd sampling line and the 10th line of the echo signal parallel to the transducer as the example, and the spectrum is shown in Figure 3. We can see that the information of the signal is repeated twice, when the length of the signal in the wavenumber domain is the same as that in the temporal domain. Thus, we can select the first half of the data in the sampling direction for beamforming, which make the amount of data be reduced to 50%. Moreover, the signal in the frequency-wavenumber domain becomes more centralized with a rapid decay. With these two features of the signal in the wavenumber domain, compressing echo signal in the wavenumber domain will lose less information than that in the temporal domain. Thus, for the same compressing rate, beamforming with compressed sensing in the wavenumber domain will obtain better image quality.

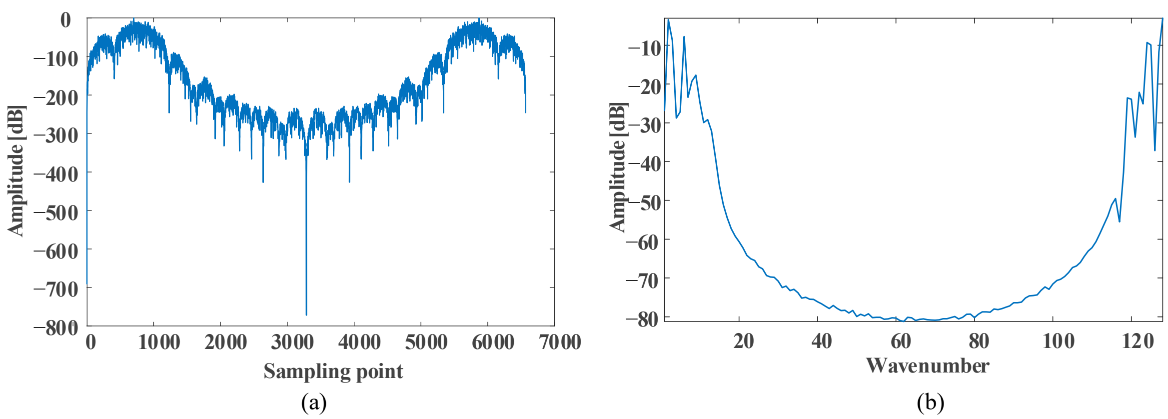

Figure 3. (**a**) Spectrum of the 32nd sampling line after FFT, (**b**) spectrum of the 10th line of echo signal parallel to transducer in the wavenumber domain after FFT.

In order to improve the image quality further, the multi-angle compound imaging method is also suitable for this framework. In this way, we introduce the general case of the algorithm, in which the plane waves are emitted at different angles. The process of this frequency-wavenumber compressive beamforming method can be summarized as follows:

1. Apply 2-dimensional FFT to the RF raw data $\psi_\theta(x, z, t)$ to transform the echo signal into the frequency-wavenumber domain as $G_\theta(k_x, z, f)$.
2. Select the first half of the data in the sampling direction for beamforming.
3. For plane waves emitted at different angles, the emission delay caused by angles should be removed by [1] at first.
4. Compress the echo signal in the Fourier domain by the sampling matrix Λ and obtain the sparse solution $\mathrm{S}(k_x)$ by RM-FOCUSS algorithm [19]. The ameliorative signal can be obtained by [12].
5. The Stolt's migration described by the procedure from [8–11] is applied with the ERM velocity $\widehat{c}$ as defined in [5].

6. Restore the data in sampling direction before inverse FFT is applied to the data after migration to transform the echo signal back to the temporal domain for imaging.

This new framework is proposed to reduce data load and memory by applying the compressive sensing on the lateral wavenumber, as well as to guarantee the quality and stability of the imaging signal after compressed sensing. The pseudo-code for tilted plane wave is shown in Figure 4. The compression rate in this frame work is discussed in Section 3 by applying this algorithm to both simulated data and in vivo experiments. Part of the information of the original echo signal will usually be lost after compressing, so the sampling matrix and the reconstruction algorithm have higher requirements to reconstruct high quality image. Therefore, the algorithm and the reconstruction algorithm can be further explored in these two aspects to find a better compressing method.

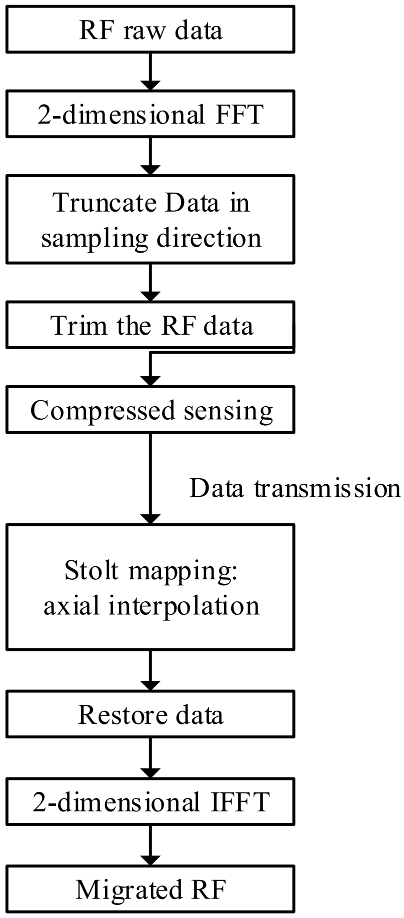

Figure 4. Diagram of wavenumber domain compressive beamforming.

2.4. Simulation Settings

Echo data were simulated by Filed II to evaluate the frame work we proposed based on the quality of the images it generates, and to compare it with DAS method and compressive beamformer in the temporal domain. Lateral resolution and contrast were the metrics to assess the image quality in this part. The metrics could be better calculated and analyzed in this part, because noise and other experimental interference could be ignored easily with the simulated data.

The numerical phantom was generated by Field II, including backscattering points and circular regions to calculate the lateral resolution and contrast. The two circular hypoechoic areas with the diameters of 5 mm and 6 mm in the phantom represented the anechoic cyst, and the two high-brightness circular areas with the same diameter simulated high-density parts in ultrasound imaging. There was a column of backscattering points arranged longitudinally and a row of scatterers arranged horizontally in the phantom. The longitudinal scattering points were used to analyze the lateral resolution of different depths.

The specifications of the research linear array transducer manufactured by Verasonics (L11-4v, Verasonics Inc., Redmond, WA, USA) were used to simulate the echo data. This is a linear array transducer with 128 elements, whose central frequency is 6.25 MHz. The pitch of transducer L11-4 is 0.3 mm and the width of each element is 0.27 mm. The transmitted signal was sampled at a rate of 50 MHz. There were 6066 samples recorded for each scanline and the image depth was 92.4 mm. The data processing was conducted using a MATLAB program (Mathworks Inc., Natick, MA, USA).

2.5. In Vivo Experiment

Organs have complicated structures and various influences on echo signal. We applied different beamformers on data obtained from the brain scan and the heart scan of the rat to analyze the performance of different beamformers. The process of the transmit and receive (T/R) for radio frequency (RF) signals was conducted using a Vantage 64 LE system (Verasonics Inc., Redmond, WA, USA), and the data processing was conducted using a MATLAB program (Mathworks Inc., Natick, MA, USA). We demonstrated the beamformers experimentally on RF data acquired linear array transducer called Vermon (Vermon Inc., Tours, France) with 128 elements. The pitch of Vermon is 0.11 mm. The central frequency is 18.8 MHz and the sampling frequency is 62.5 MHz. Vermon is a transducer specially designed for animals. The in vivo rat experiment was performed according to the Suzhou Institute of Biomedical Engineering and Technology (Chinese Academy of Sciences) Institutional Animal Ethics Committee (SibetAEC) protocol (2021-B22). We used female rats of SPF degree which were cultivated by 8 weeks.

3. Results

3.1. Compared with DAS and Stolt's f-k Method

To analyze the performance of the new beamforming method in B mode ultrasound imaging, the point scatterers at different depth were used to calculate resolution, and the hypoechoic region centered at (−5, 40) mm and the strong reflected regions centered at (−5, 70) mm were used to calculate different kinds of contrast. As it shows in Figure 4, the 6 mm radius cyst called region A is used to analyze the contrast of hypoechoic. The region B with 6 mm diameter is used to analyze the contrast of strong reflected region. Region C in the red square is used as the background to calculate the contrast. The horizontal resolution is analyzed by the point scatterer at different positions. After evaluating the performance of the algorithm in simulation, the in vivo plane wave measurements were executed by Verasonics research scanner (Vermon Inc., Tours, France) in Section 4. The contrast was represented by gCNR, which was defined as [37]

$$gCNR = 1 - \int_{-\infty}^{\infty} \min_x \{p_t(x), p_b(x)\} dx \tag{21}$$

where $p_t(x)$ is the probability density distribution in the target region A and region B, and $p_b(x)$ is the probability density distribution of background region C.

The performance of wavenumber domain beamforming is evaluated in two aspects. The first is to compare the image quality with DAS. The second part is to compare the image quality with strictly consistent condition and the same compressed rate, so as to assess the stability of the algorithm and the performance of compressed sensing in the wavenumber domain compared with that in the temporal domain. Multi-angle RF coherent compounding can be applied on both DAS and beamforming in the wavenumber domain to further improve image quality. However, in order to eliminate the influence of the number of angles on the image quality, we simulated only one plane wave on angle 0° to perform different beamforming algorithms in this section.

We compared the compressive beamforming with Stolt's f-k migration (represented by fkCS in the image) with DAS to evaluate the performance of the new process by image quality, as well as compared with non-compressive framework. In Section 3.1, the image quality was evaluated and compared with the compression rate $R = 80\%$ in fkCS (abbreviated as fkCS_80%), and the simulated result is shown in Figure 5 with a dynamic range of 50 dB. The compression rate is defined as

$$R = \frac{N_c}{N_o} \times 100\% \tag{22}$$

where N_c and N_o are the amount of data after and before compressed sensing, respectively. In this part, the image quality is evaluated from different views. Firstly, the lateral resolution is measured at different depths. Secondly, the contrast of cyst and high reflection region are calculated and represented by $gCNR$.

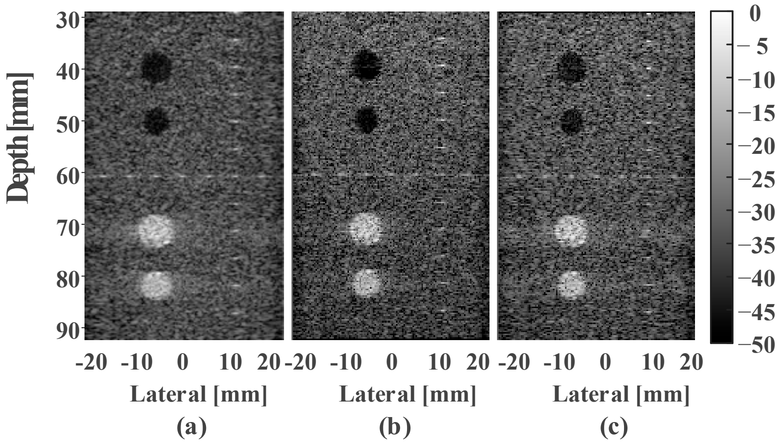

Figure 5. Simulated images by (**a**) DAS, (**b**) fk and (**c**) fkCS with 80% compression rate with hypoechoic, bright region and point scatterers.

The point scatterers in the region D at the depth from 30 mm to 85 mm were involved to analyze the lateral resolution at different depths. The lateral resolution was estimated by measuring the full-width at half maximum (FWHM) of the envelop of the signal after beamforming. The effect of different depths on lateral resolution with different beamformers is shown in Figure 6. As shown in Figure 6, the compressive beamforming in the wavenumber domain provides comparable or better lateral resolution than DAS, when the data load has been compressed to 80%, especially with increase of the depth. In this study, we use dynamic aperture in the DAS beamformer with Hanning window to improve the lateral resolution in near field. However, the resolutions of DAS in near field still not match that of fkCS, whose compression rate is 80%. With the depth increase, the resolutions of three imaging method are comparable, but the resolutions vary in deep place. Consequently, lateral resolution of beamformer in the Fourier domain perform better in near field and deep place. The contrast of three beamformers is shown in Table 1. With the 20% reduction of data, the lateral resolution and contrast of fkCS are comparable to the results of Stolt's f-k beamformer, and the results of hypoechoic are better than that of DAS. The gCNR of DAS of bright region is a little better and there are some artifacts around bright regions, which is because the Hanning window widens the main lobe of the signal when decreases the sidelobe.

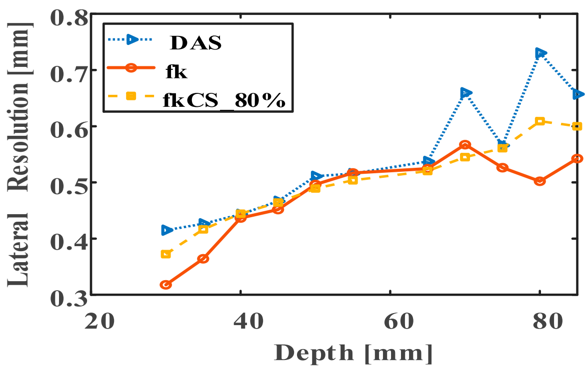

Figure 6. Effect of depth on the lateral resolution.

Table 1. Contrast of DAS, Stolt's f-k and proposed framework.

	gCNR	
	Hypoechoic	**Bright Region**
DAS	0.8429	0.9385
fk	0.9035	0.8874
fkCS_80%	0.8529	0.8917

3.2. Compared with Compressive Beamformer in the Temporal Domain

To analyze the performance of compressive beamforming method in the wavenumber domain based on Stolt's f-k migration (fkCS), we compared the new framework with the conventional beamforming based on compressed sensing in the temporal domain. To reduce the influence of different beamformers on image quality, the algorithm of control group still uses Stolt's f-k migration during beamforming, but the compressed sensing is applied to the echo signal before FFT, which means the signal in the temporal domain is compressed. This framework of the control group is called beamformer in the temporal domain based on compressed sensing (abbreviated as tmCS). The lateral resolution and contrast were calculated by the simulated data at different compression rates. The compression rate decreases from 100% to 20% to analyze the changes of the lateral resolution and contrast. The B mode images after two kinds of beamformers are shown as Figure 7d,e, whose compression rate is 50%.

With the decrease in compression rate, the beamformer will take up less memory and less transmission space. However, the information will be lost as well. From B mode images generated by fkCS in Figure 7d and by tmCS in Figure 7e with a dynamic range of 50 dB, artifacts appear due to the loss of information with the compression rate of 50%. It can be seen from the B-mode images that at a compression rate of 50%, the image quality of fkCS is significantly better than that of tmCS. As shown in Figure 7e, when the amount of the signal is compressed to 50%, the low echo signal will be almost covered and the high intensity signal will produce artifact. Since the image of tmCS loses half of the signal during the compression process in the temporal domain, it is more dependent on the nearby signal when the reconstruction algorithm restores the image. Thus, the low-echo signal will be covered by the surrounding signal, and the high-intensity signal will affect the surrounding signal and produce artifacts. In the Fourier domain, due to the symmetry of the Fourier-transformed signal, the signal can retain more effective information during compression and reduce the generation of noise and artifacts during reconstruction of signal.

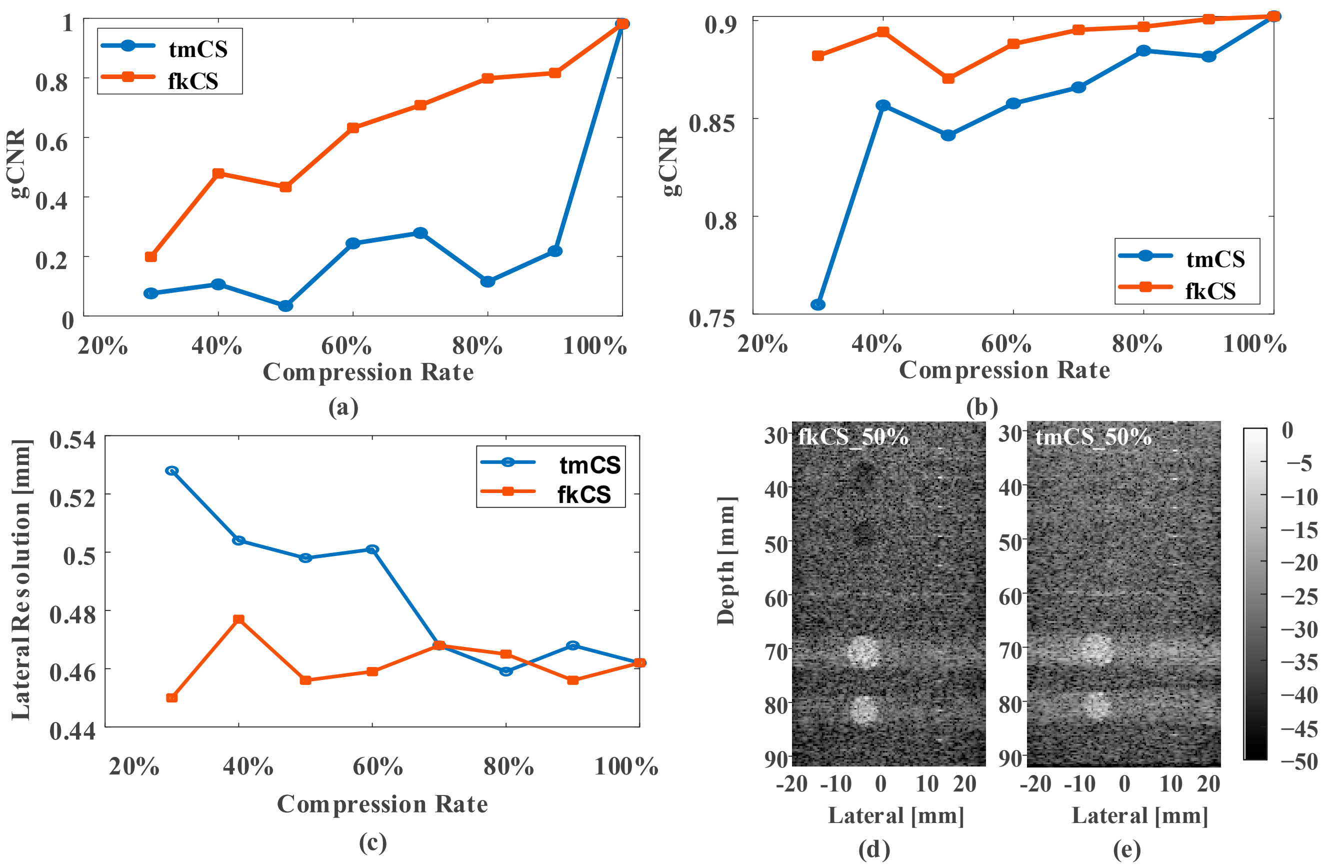

Figure 7. Contrasts and lateral resolutions with different compression rates, as well as B mode images generated by fkCS and tmCS beamforming with hypoechoic, bright region and point scatterers: (**a**) contrast of cyst, (**b**) contrast of strong reflection region, (**c**) lateral resolution, (**d**) B mode image of fkCS with 50% compression rate, (**e**) B mode image of tmCS 50% compression rate.

Figure 7c shows effects of compression rate on lateral resolution. In order to reduce the influence of artifacts of strong reflection area, we choose the point scatterer at (10, 45) mm to measure resolution. From Figure 7c we can see that the lateral resolutions are comparable when the compression rate is above 70%. When the compression rate decreases sequentially, the FWHM of tmCS increases rapidly, while the resolution of fkCS fluctuates slightly. The image quality of tmCS deteriorates more rapidly because more information is lost during compression than that in fkCS.

3.3. Results on Brain Scan

Organs have complicated structures and various influences on echo signal. We firstly apply different beamformers on data obtained from the brain scan of the rat to analyze the performance of different beamformers during imaging for static organ. The brain scan B mode images with 60 dB dynamic range based on different beamformers are shown in Figure 8. The peak signal-to-noise ratio (PSNR) was calculated by area A and area B in Figure 8, which contains the top and bottom contour of the brain to evaluate the ability of retaining effective information and removing noise. Area C is the background signal used to calculate PSNR. The results are shown in Table 2.

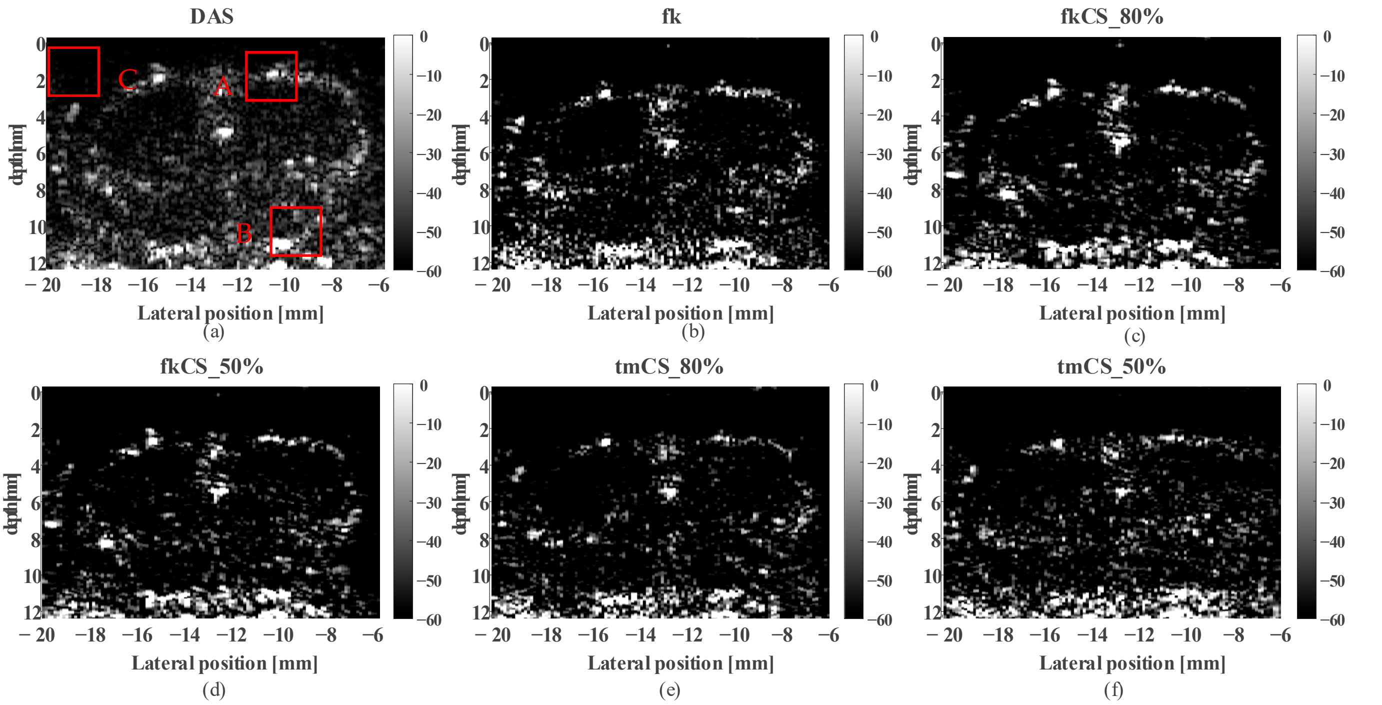

Figure 8. B mode images of rat brain scan based on different beamformers: (**a**) DAS, (**b**) Stolt's f-k, (**c**) fkCS with compression rate of 80%, (**d**) fkCS with compression rate of 50%, (**e**,**f**) are tmCS with compression rates of 80% and 50%, respectively.

Table 2. PSNR of brain scan experiment.

Beamformer	PSNR (dB)	
	Top Edge of the Brain	Bottom Edge of the Brain
DAS	11.7774	17.9290
fk	17.8474	15.1833
fkCS_80%	17.6321	14.3764
fkCS_50%	16.6327	14.3707
tmCS_80%	16.3555	14.8068
tmCS_50%	15.3797	14.1903

The PSNR is expressed as follows:

$$PSNR = 20\log_{20}\left(\frac{MAX_I}{\sqrt{MSE}}\right) \tag{23}$$

where MAX_I is the maximum value of signal and MSE is the mean-square error of the signal. The PSNR of the top contour of the brain based on fk and fkCS with 80% compression rate is the best. When the compression rate is the same, PSNR of fkCS is better than that of tmCS, which means the ability of eliminating noise of compressive beamformer in the Fourier domain is better as well. It can be seen from Figure 8a that in the image based on the DAS, the echo signal of rat's bottom skull is strong, which influences the brain signal. This leads to high PSNR of bottom edge and low PSNR of top edge of the brain in Table 2. This result is consistent with simulated results, which the ability of DAS to eliminate high refection noise is weaker than beamforming in the Fourier domain.

3.4. Results on Heart Scan

Heart scan requires higher frame rate of the ultrasonic device. Compressive beamforming in the Fourier domain provides a method for echo signal data to take up less space and achieves a higher transfer speed. This experiment is to assess performance of beamformers based on high frame rate plane wave imaging. The experimental results whose dynamic range of 55 dB based on different beamformers are shown in Figure 9. It can be seen from Figure 9a that in the image based on the DAS, the contour of the upper edge of the heart is the least obvious. The PSNR was calculated by area A in Figure 9 which contains the contour of the heart. The results are shown in Table 3. The PSNR of the image after compression performs better than that of DAS and before compression, because compressed sensing process help to eliminate part of noise by making the signal sparse.

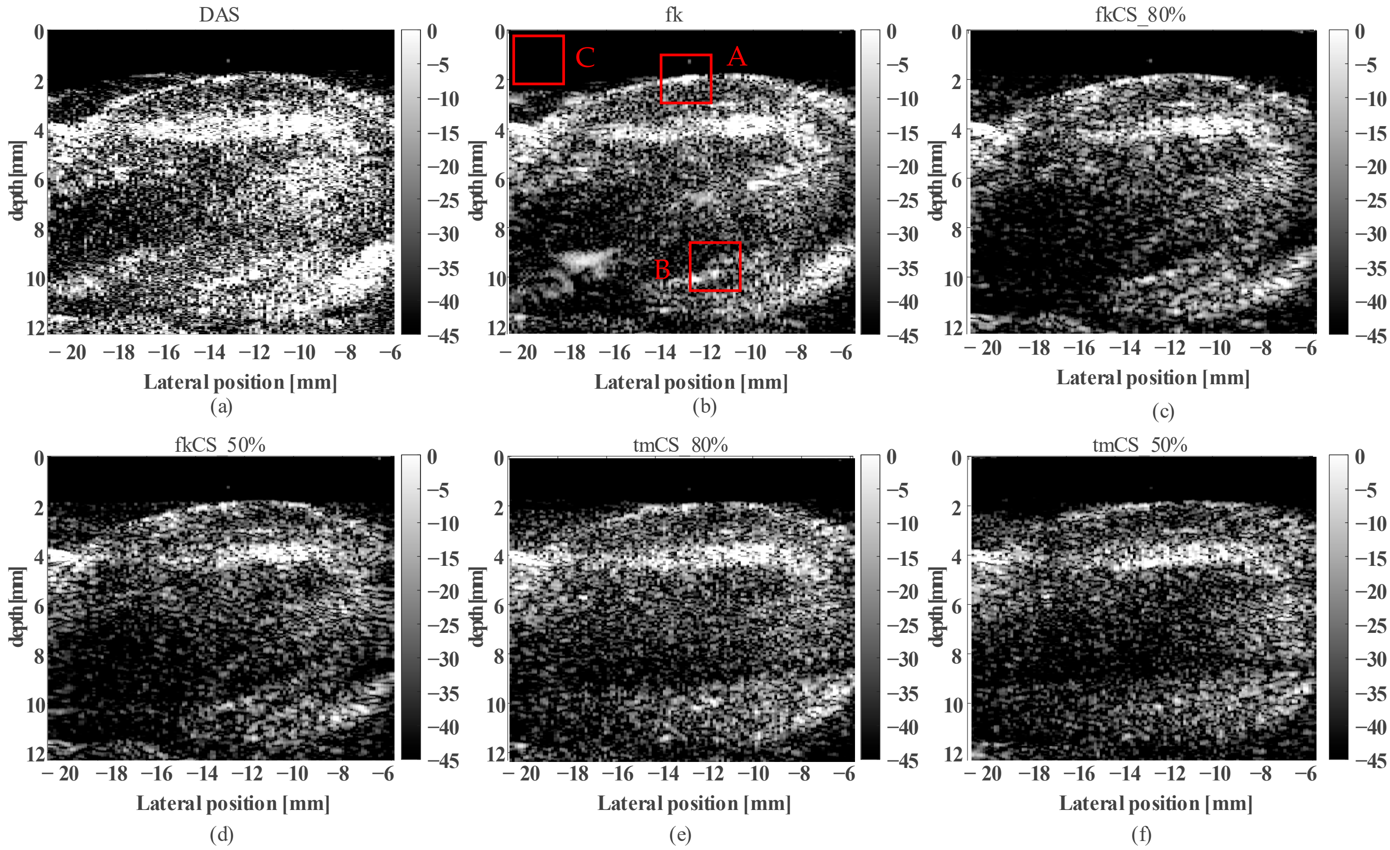

Figure 9. B mode images based on different beamformers: (**a**) DAS, (**b**) Stolt's f-k, (**c**) fkCS with compression rate of 80%, (**d**) fkCS with compression rate of 50%, (**e**,**f**) are tmCS with compression rates of 80% and 50%, respectively.

Table 3. PSNR of different beamformers on heart scan.

Beamformer	PSNR (dB)	
	Contour of Heart	Contour of Cardiac Chamber
DAS	15.9920	17.5155
fk	18.8017	16.0897
fkCS_80%	17.9650	15.3046
fkCS_50%	17.4662	13.3454
tmCS_80%	12.4989	11.0023
tmCS_50%	12.4318	11.4359

The strong reflection signal in the bottom affects the imaging of the cardiac chamber, causing the bottom contour of the cardiac chamber to be covered by the strong reflection signal. The area B in Figure 9 which contains the bottom edge of the cardiac chamber, is used to calculate the PSNR. The contour of the cardiac chamber is the most obvious in the imaging results based on the algorithms fk and fkCS. The upper edge of the cardiac chamber of the tmCS image can be seen, and the signal at the bottom edge is almost lost. The results of in vivo experiments are similar to that of simulation. Compressive beamformer in the wavenumber domain provides more stable imaging process with less data load.

4. Discussion

4.1. Influence of Number of Angles on Compressive Beamformer in the Fourier Domain

Beamformers in the Fourier domain based on Stolt's f-k migration are compatible with multi-angle RF coherent compounding imaging method [21]. Then compressive beamformer in the Fourier domain is also available for multi-angle compounding imaging. Although the results of fkCS is better than DAS, the image quality will be influenced with a low compression rate. Multi-angle compounding imaging is a method to improve image quality from the signal transmitter. In this part, we discuss the influence of the number of angles on compressive beamforming framework in the wavenumber domain with different compression rates, as well as comparing with compressive beamforming in the temporal domain.

Image quality was analyzed by lateral resolution and contrasts. As it shown in Figure 10, lateral resolution was measured by point scatterer located at (10, 40) mm. Contrasts of cyst and strong reflection region were measured with area A and area B in Figure 5. We discussed the influence of number of angles with Stolt's f-k migration method and compressive method with compression rates of 30%, 50% and 80%, which was represented by fk, fkCS_80%, fkCS_50% and fkCS_30%, respectively. The simulated B mode images with 5 angles were shown in Figure 10d–g, respectively. It can be seen that when compression rate decreases to 30%, the strong reflection region will distort significantly.

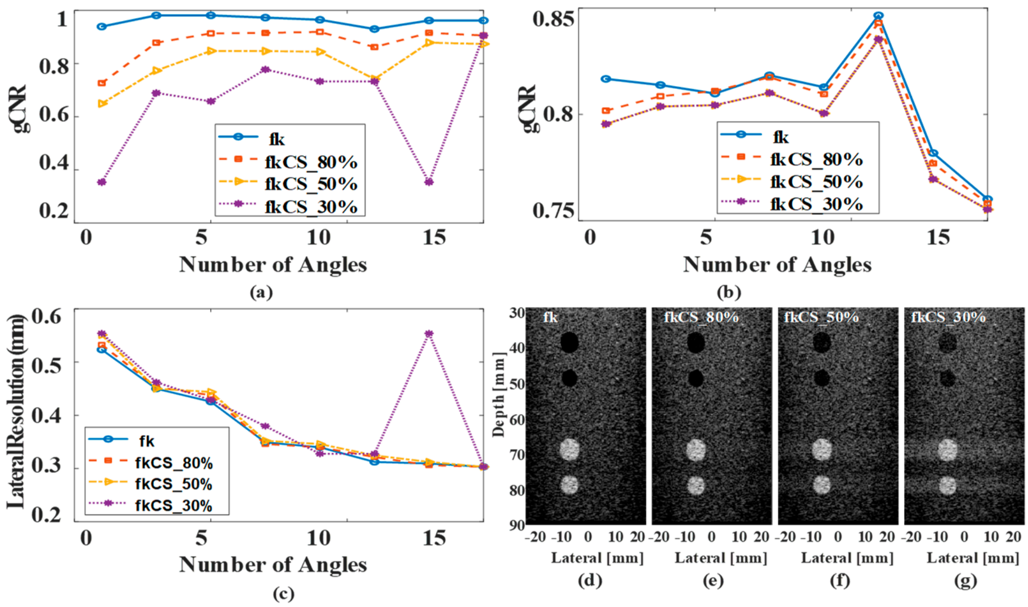

Figure 10. Influence of number of angles on fkCS. (**a**) gCNR of cyst, (**b**) gCNR of strong reflection area, (**c**) lateral resolution with different number of angles and compression rate, (**d**–**g**) are B mode images based on beamformer of Stolt's f-k, and fkCS with compression of 80%, 50% and 30% with 40 dB dynamic range, respectively.

As shown in Figure 10, with the increase in the number of compounding angles, the lateral resolution and low echo contrast of images generated by different methods have improved, but the degree of improvement is limited. The main influence of number of angles on contrast is about low echo area. From Figure 10a, when the number of angles is less than 5, increasing the number of angles can significantly improve the cyst contrast. Additionally, the lower the compression rate, the more obvious the effect of the increase of the angle. With the decrease in compression rate, the contrast of cyst deteriorates, especially the change of contrast is unstable with compression rate of 30%. For the lateral resolution shown in Figure 10c, when the number of angles is less than 12, the increase in the number of angles can improve the lateral resolution, but the number of angles has similar effects on images with different compression rates. When the number of angles is greater than 11, increasing the number of angles will not improve the lateral resolution area any more. At this time, the increase in the number of composite angles will not improve the image quality, but will reduce the frame rate.

4.2. Memory Occupation, Computational Complexity and Telemedicine Imaging Speed

The compressive beamforming in the Fourier domain is especially practical for tele-ultrasound imaging, which puts forward a high requirement for imaging speed and data transfer speed. In this part, we discuss the memory occupation, computational complexity and transfer speed.

The main difference between the compressive beamformer on the lateral wavenumber and on the sampling direction is the measurement matrix, which occupies memory and increases the computational complexity during matrix calculation as well. The measurement matrix $\mathrm{P} = \Lambda\mathrm{H}$ can be calculated by sampling matrix Λ and the transfer matrix H. We define N as the number of elements in the transducer and Ns as the number of time samples (typically ≥ 1000). In the proposed beamformer, for the compression rate of R, the dimension of sampling matrix Λ on lateral wavenumber is $RN \times N$. The dimension of transfer matrix H on the lateral direction in [14] is $N \times 2N$. Then the dimension of the measurement matrix is $RN \times 2N$. If we apply the compressed sensing on the axial wavenumber, the dimension of the sampling matrix is $RNs \times Ns$ and the dimension of the transfer matrix is $Ns \times 2Ns$, where R is the compression rate. The transfer matrix H is still generated by [13,14]. The measurement matrix is $RNs \times 2Ns$ in final. Since Ns is usually many times larger then N, the compressed sensing on the sampling direction will occupy more memory than that of the lateral wavenumber.

The compressed sensing has been applied on DAS [33] and on Fourier-domain beamforming on the sampling direction [37]. To compare the computational complexity of different beamformers, we assume that the compressed sensing model applied on different beamformers is the same. In comparison, the computation complexity of the DAS proposed by Montaldo et al. is $O(N^2Ns)$, and the computation complexity of beamformer in the wavenumber domain based on Stolt's f-k migration is decreased to $O(N \cdot Ns \log(N \cdot Ns))$ [21]. For the Fourier domain beamforming proposed by *Chernyakova* et al. [30,31], Fourier series coefficients $c[k]$, which can be generated by the distortion function $q_{k,m}(t,\theta)$, is the key factor to reconstruct the ultrasound image. It must retrieve $O(N(N \cdot Ns \cdot K + Ns \cdot K))$ interpolated data to calculate the distortion function and Fourier series coefficients, where K is the number of Fourier series coefficients, and then perform $O(N \cdot Ns)$ summations. This method achieves sub-Nyquist frequency-domain beamforming, but increases the computational complexity to $O(N^2 \cdot Ns \cdot K)$. Thus, the computation complexity of beamformer in the wavenumber domain based on Stolt's f-k migration has benefits on reducing computational complexity.

To evaluate the telemedicine imaging speed, we obtained the raw RF data from the Vantage 64 LE system, whose frame rate of data acquisition is 500 frame/s. When data compression is performed, the data acquisition frame rate will drop to 200 frame/s. Then raw data is compressed the and is transmitted to PC for final imaging. For the raw data containing 1000 frames of ultrasound images, the file size is 454.3 MB. The signal processing steps, including filter, beamforming, and Hilbert transformation are done on the PC. The time required to acquire one ultrasound image after averaging via telemedicine with DAS and fkCS method is shown in Figure 11. The time of data acquisition is a little longer because of compression process, but the time of data transmission is greatly reduced.

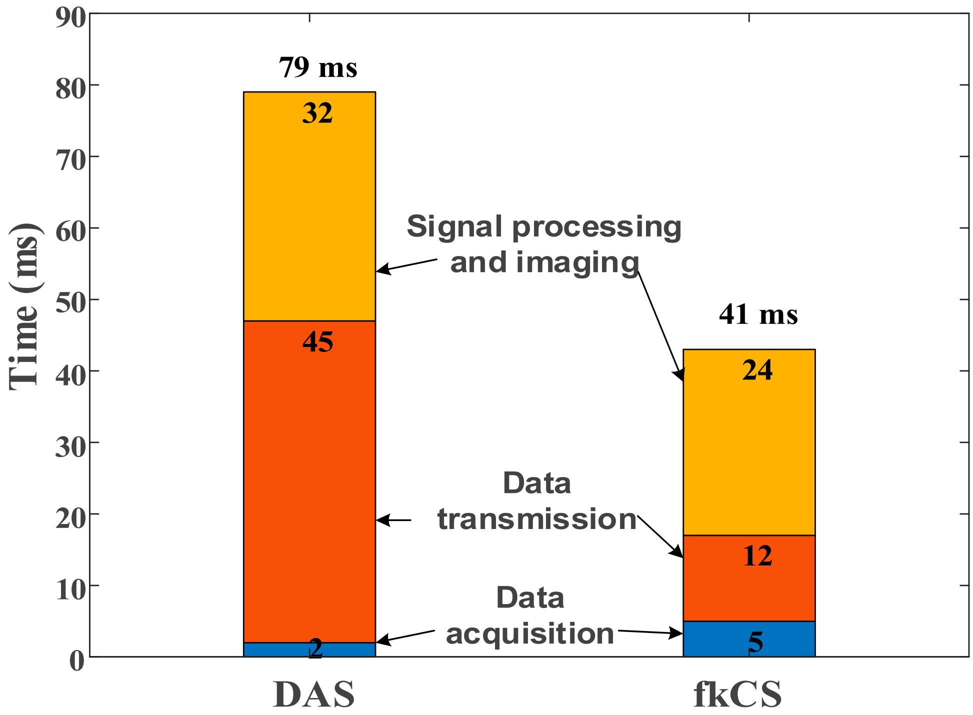

Figure 11. The time required to acquire one ultrasound image after averaging.

4.3. Limitations and Future Works

Despite the high resolution and contrast compared with DAS, the image quality based on fkCS is not as good as beamformers based on MV, especially with low compression rate. It can be seen in Figure 10g that there are artifacts around the bright region when the compression rate decrease to 30%. Even compound imaging cannot eliminate these artifacts. In order to further improve the image quality, more research can be conducted in the compression process and reconstruction algorithm. A good compression process can not only compress the data load with a lower compression rate, but also improve the image quality after recovery. In this paper, we chose discrete sinusoidal as the sparse basis and the Gaussian matrix to construct the sampling matrix. The restoration algorithm is the re-weight minimum-focal underdetermined system solver algorithm (RM-FOCUSS). There are many studies in this field which can be combined with plane wave beamforming to improve the image quality.

In addition, this method is only available with plane wave emitted by linear array transducer. For the diverge wave emitted by curve array transducer, Stolt's f-k migration is not suitable anymore due to the phase shift. Curve array transducers are widely used in practice, so it makes sense to combine the compressive beamforming with a migration method suitable for diverge wave.

5. Conclusions

In this paper, we propose a compressive beamforming method in the Fourier domain based on Stolt's f-k migration. This framework combines the advantages of beamforming in the Fourier domain and compressed sensing theory to provide a higher transmission rate and better image quality during tele-ultrasound imaging, especially for ultrasound cardiac imaging. Therefore, compared with DAS and beamformers with compressed sensing in the temporal domain, this framework improves contrast and lateral resolution of the ultrasound image while reducing data load during transmission and beamforming. Moreover, the method compresses data load by cutting down the number of transducer elements, which does not require too much memory for measurement matrix during sparsity and compression. Our work illustrates that the compressive beamforming on lateral wavenumber is a competitive method which is especially useful to increase data transfer speed and imaging speed.

Author Contributions: Conceptualization, X.Z. and Y.J.; methodology, X.Z.; software, N.W.; data curation, Y.X.; writing—original draft preparation, X.Z.; writing—review and editing, Y.J. and Y.C. All authors have read and agreed to the published version of the manuscript.

Funding: This work was supported in part by the National Natural Science Foundation of China (Grant NO. 21927803), National Key Research and Development Program of China (Grant NO. 2019YFC0120500), Jiangsu Science and Technology Project (Grant NO. BZ2021037), the Funds of Youth Innovation Promotion Association, Chinese Academy of Sciences (Grant NO. Y201961 and 20A122062ZY), Suzhou Science and Technology Project (Grant NO. SS202062), Key R&D program of Jiangsu Province (Grant NO. BE2021659), Suzhou science and technology plan project (Grant NO. SZS201903).

Institutional Review Board Statement: The animal study protocol was approved by the Suzhou Institute of Biomedical Engineering and Technology (Chinese Academy of Sciences) Institutional Animal Ethics Committee (SibetAEC) (protocol code: 2021-B22).

Informed Consent Statement: Not applicable.

Data Availability Statement: Not applicable.

Conflicts of Interest: The authors declare no conflict of interest.

References

1. Recker, F.; Hoehne, E.; Damjanovic, D.; Schaefer, V.S. Ultrasound in Telemedicine: A Brief Overview. *Appl. Sci.* **2022**, *12*, 958. [CrossRef]
2. Chan, F.Y.; Whitehall, J.; Hayes, L.; Taylor, A.; Soong, B.; Lessing, K.; Cincotta, R.; Cooper, D.; Stone, M.; Lee-Tannock, A.; et al. Minimum requirements for remote realtime fetal tele-ultrasound consultation. *J. Telemed. Telecare* **1999**, *5*, 171–176. [CrossRef] [PubMed]
3. Liteplo, A.; Noble, V.; Attwood, B. Real-time video transmission of ultrasound images to an iPhone. *Crit. Ultrasound J.* **2010**, *1*, 105–110. [CrossRef]
4. Bercoff, J.; Tanter, M.; Fink, M. Supersonic shear imaging: A new technique for soft tissue elasticity mapping. *IEEE Trans. Ultrason. Ferroelectr. Freq. Control* **2004**, *51*, 396–409. [CrossRef] [PubMed]
5. Errico, C.; Pierre, J.; Pezet, S.; Desailly, Y.; Lenkei, Z.; Couture, O.; Tanter, M. Ultrafast ultrasound localization microscopy for deep super-resolution vascular imaging. *Nature* **2015**, *527*, 499–502. [CrossRef] [PubMed]
6. Lu, J.Y. 2D and 3D high frame rate imaging with limited diffraction beams. *IEEE Trans. Ultrason. Ferroelectr. Freq. Control* **1997**, *44*, 839–856. [CrossRef]
7. Tanter, M.; Fink, M. Ultrafast Imaging in Biomedical Ultrasound. *IEEE Trans. Ultrason. Ferroelectr. Freq. Control* **2014**, *61*, 102–119. [CrossRef]
8. Bercoff, J. *Ultrafast Ultrasound Imaging*; Elsevier Inc.: Amsterdam, The Netherlands, 2011.
9. Montaldo, G.; Tanter, M.; Bercoff, J.; Benech, N.; Fink, M. Coherent Plane-Wave Compounding for Very High Frame Rate Ultrasonography and Transient Elastography. *IEEE Trans. Ultrason. Ferroelectr. Freq. Control* **2009**, *56*, 489–506. [CrossRef]
10. Mace, E.; Montaldo, G.; Osmanski, B.F.; Cohen, I.; Fink, M.; Tanter, M. Functional Ultrasound Imaging of the Brain: Theory and Basic Principles. *IEEE Trans. Ultrason. Ferroelectr. Freq. Control* **2013**, *60*, 492–506. [CrossRef]
11. Capon, J. High-Resolution Frequency-Wavenumber Spectrum Analysis. *Proc. IEEE* **1969**, *57*, 1408–1418. [CrossRef]
12. Moubark, A.M.; Alomari, Z.; Harput, S.; Cowell, D.M.J.; Freear, S. Enhancement of contrast and resolution of B-mode plane wave imaging (PWI) with non-linear filtered delay multiply and sum (FDMAS) beamforming. In Proceedings of the 2016 IEEE International Ultrasonics Symposium (IUS), Tours, France, 18–21 September 2016; p. 4. [CrossRef]
13. Synnevåg, J.F.; Austeng, A.; Holm, S. Adaptive beamforming applied to medical ultrasound imaging. *IEEE Trans. Ultrason. Ferroelectr. Freq. Control* **2007**, *54*, 1606–1613. [CrossRef] [PubMed]
14. Paridar, R.; Asl, B.M. Plane wave ultrasound imaging using compressive sensing and minimum variance beamforming. *Ultrasonics* **2023**, *127*, 106838. [CrossRef] [PubMed]
15. Luijten, B.; Cohen, R.; de Bruijn, F.J.; Schmeitz, H.A.W.; Mischi, M.; Eldar, Y.C.; van Sloun, R.J.G. Adaptive Ultrasound Beamforming Using Deep Learning. *IEEE Trans. Med. Imaging* **2020**, *39*, 3967–3978. [CrossRef] [PubMed]
16. Tierney, J.; Luchies, A.; Khan, C.; Baker, J.; Brown, D.; Byram, B.; Berger, M. Training Deep Network Ultrasound Beamformers With Unlabeled In Vivo Data. *IEEE Trans. Med. Imaging* **2022**, *41*, 158–171. [CrossRef]
17. Gao, J.L.; Xu, L.; Zou, Q.; Zhang, B.; Wang, D.Y.; Wan, M.X. A progressively dual reconstruction network for plane wave beamforming with both paired and unpaired training data. *Ultrasonics* **2023**, *127*, 106833. [CrossRef]

18. Lu, J.Y. Experimental study of high frame rate imaging with limited diffraction beams. *IEEE Trans. Ultrason. Ferroelectr. Freq. Control* **1998**, *45*, 84–97. [CrossRef]
19. Kruizinga, P.; Mastik, F.; de Jong, N.; van der Steen, A.F.W.; van Soest, G. Plane-Wave Ultrasound Beamforming Using a Nonuniform Fast Fourier Transform. *IEEE Trans. Ultrason. Ferroelectr. Freq. Control* **2012**, *59*, 2684–2691. [CrossRef]
20. Bernard, O.; Zhang, M.M.; Varray, F.; Gueth, P.; Thiran, J.P.; Liebgott, H.; Friboulet, D. Ultrasound Fourier Slice Imaging: A novel approach for ultrafast imaging technique. In Proceedings of the IEEE International Ultrasonics Symposium (IUS), Chicago, IL, USA, 3–6 September 2014; pp. 129–132.
21. Garcia, D.; Le Tarnec, L.; Muth, S.; Montagnon, E.; Poree, J.; Cloutier, G. Stolt's f-k Migration for Plane Wave Ultrasound Imaging. *IEEE Trans. Ultrason. Ferroelectr. Freq. Control* **2013**, *60*, 1853–1867. [CrossRef]
22. Stolt, R.H. Migration By Fourier-Transform. *Geophysics* **1978**, *43*, 23–48. [CrossRef]
23. Chen, C.; Hendriks, G.; van Sloun, R.J.G.; Hansen, H.H.G.; de Korte, C.L. Improved Plane-Wave Ultrasound Beamforming by Incorporating Angular Weighting and Coherent Compounding in Fourier Domain. *IEEE Trans. Ultrason. Ferroelectr. Freq. Control* **2018**, *65*, 749–765. [CrossRef]
24. Chen, Y.; Xiong, Z.H.; Kong, Q.R.; Ma, X.X.; Chen, M.; Lu, C. Circular statistics vector for improving coherent plane wave compounding image in Fourier domain. *Ultrasonics* **2023**, *128*, 106856. [CrossRef]
25. Donoho, D.L. Compressed sensing. *IEEE Trans. Inf. Theory* **2006**, *52*, 1289–1306. [CrossRef]
26. Lu, C.-W.; Liu, X.-J.; Fang, G.-Y. Compressive Sensing for GPR Data Acquisition. *Acta Electron. Sin.* **2011**, *39*, 2204–2206.
27. Herman, M.; Strohmer, T. Compressed sensing radar. In Proceedings of the 33rd IEEE International Conference on Acoustics, Speech and Signal Processing, Las Vegas, NV, USA, 30 March–4 April 2008; pp. 1509–1512.
28. Wang, C.Z.; Peng, X.; Liang, D.; Xiao, Y.; Qiu, W.B.; Qian, M.; Zheng, H.R. An Easily-achieved Time-domain Beamformer for Ultrafast Ultrasound Imaging Based on Compressive Sensing. In Proceedings of the 37th Annual International Conference of the IEEE-Engineering-in-Medicine-and-Biology-Society (EMBC), Milan, Italy, 25–29 August 2015; pp. 7490–7493.
29. Szasz, T.; Basarab, A.; Kouame, D. Beamforming Through Regularized Inverse Problems in Ultrasound Medical Imaging. *IEEE Trans. Ultrason. Ferroelectr. Freq. Control* **2016**, *63*, 2031–2044. [CrossRef] [PubMed]
30. Chernyakova, T.; Eldar, Y.C. Fourier-Domain Beamforming: The Path to Compressed Ultrasound Imaging. *IEEE Trans. Ultrason. Ferroelectr. Freq. Control* **2014**, *61*, 1252–1267. [CrossRef]
31. Chernyakova, T.; Cohen, R.; Mulayoff, R.; Sde-Chen, Y.; Fraschini, C.; Bercoff, J.; Eldar, Y.C. Fourier-Domain Beamforming and Structure-Based Reconstruction for Plane-Wave Imaging. *IEEE Trans. Ultrason. Ferroelectr. Freq. Control* **2018**, *65*, 1810–1821. [CrossRef]
32. Besson, A.; Zhang, M.M.; Varray, F.; Liebgott, H.; Friboulet, D.; Wiaux, Y.; Thiran, J.P.; Carrillo, R.E.; Bernard, O. A Sparse Reconstruction Framework for Fourier-Based Plane-Wave Imaging. *IEEE Trans. Ultrason. Ferroelectr. Freq. Control* **2016**, *63*, 2092–2106. [CrossRef]
33. Besson, A.; Carrillo, R.E.; Bernard, O.; Wiaux, Y.; Thiran, J.P. Compressed Delay-And-Sum Beamforming For Ultrafast Ultrasound Imaging. In Proceedings of the 23rd IEEE International Conference on Image Processing (ICIP), Phoenix, AZ, USA, 25–28 September 2016; pp. 2509–2513.
34. Gorodnitsky, I.F.; Rao, B.D. Sparse signal reconstruction from limited data using FOCUSS: A re-weighted minimum norm algorithm. *IEEE Trans. Signal Process.* **1997**, *45*, 600–616. [CrossRef]
35. Candes, E.J. The restricted isometry property and its implications for compressed sensing. *Comptes Rendus Math.* **2008**, *346*, 589–592. [CrossRef]
36. Candes, E.; Romberg, J. Signal recovery from random projections. In Proceedings of the Conference on Computational Imaging III, San Jose, CA, USA, 17–18 January 2005; pp. 76–86.
37. Rodriguez-Molares, A.; Rindal, O.M.H.; D'Hooge, J.; Masoy, S.E.; Austeng, A.; Bell, M.A.L.; Torp, H. The Generalized Contrast-to-Noise Ratio: A Formal Definition for Lesion Detectability. *IEEE Trans. Ultrason. Ferroelectr. Freq. Control* **2020**, *67*, 745–759. [CrossRef]